

Characterization and enhanced photocatalytic performance of nanocrystalline Ni-substituted Zn ferrites synthesized by DEA-assisted sol–gel auto-combustion method

Thanit Tangcharoen · Anucha Ruangphanit ·
Wantana Klysubun · Wisanu Pecharapa

Received: 16 November 2012 / Accepted: 19 March 2013 / Published online: 26 March 2013
© Springer Science+Business Media New York 2013

Abstract Nanocrystalline Ni-substituted Zn ferrites with compositions of $\text{Ni}_x\text{Zn}_{1-x}\text{Fe}_2\text{O}_4$ ($x = 0\text{--}1.0$) were synthesized by sol–gel auto-combustion method using metal nitrate as the reactants. Diethanolamine was selected as the fuel instead of conventional fuels such as urea, citric acid, tartaric acid or glycine. Characterization of after-calcined ferrite samples were conducted in terms of crystal structure, molecular vibrations, morphology and magnetic properties through X-ray diffraction, Fourier transform infrared spectroscopy, scanning electron microscope and vibrating sample magnetometer analysis, respectively. The photocatalytic activities of these ferrites were studied in term of degradation of Rhodamine B under daylight-irradiation. The corresponding results indicate that nickel loading content has significant effect on physical, magnetic, optical and photocatalytic properties of the ferrite. Comparing to the undoped Zn ferrite, $\text{Ni}_{0.6}\text{Zn}_{0.4}\text{Fe}_2\text{O}_4$ shows the enhancement in photocatalytic activity accompanying the degradation of Rhodamine B aqueous solution up to 77 % within 4 h. The result suggests the feasibility of

this material as potential sunlight-activated photocatalyst in wastewater treatment and environment cleaning applications.

Keywords Ferrites · Sol–gel auto-combustion · Diethanolamine · Photocatalyst

1 Introduction

Nickel Zinc ferrite is one of the most important ferrites which has an inverse spinel cubic crystal structure [1]. It is one kind of ferrimagnetic materials which present ferrimagnetism initiated from the magnetic moment of anti-parallel spins between Fe^{3+} ions at tetrahedral sites (A sites) and Ni^{2+} ions at octahedral sites (B sites) [1]. The general formula of ferrite is AB_2O_4 , where A is the divalent ion such as Ni^{2+} , Zn^{2+} , Mg^{2+} , Fe^{2+} , Mn^{2+} or Co^{2+} and B is Fe^{3+} which can be replaced by the other trivalent ions such as Al^{3+} , Co^{3+} or Cr^{3+} [2]. This is very important raw material for various manufacturing applications due to its multipurpose and outstanding properties such as high resistivity, high dielectric, high initial permeability, high saturation magnetization, thermal stability, low eddy current losses, super paramagnetic phenomenon and flexible configuration [3–10]. It has been widely used in electronic devices, computer devices, transportation, communication, military munitions, space exploration and even medication [10–14]. In addition, there are a number of research reports that took the potential of ferrites to remove wasted dyes in polluted water from industries [15]. It is typically notified that microstructure, magnetic and electrical properties of ferrites are highly sensitive to composition, additive, grain size, impurities and the arrangement [16].

T. Tangcharoen · W. Pecharapa (✉)
College of Nanotechnology, King Mongkut's Institute of
Technology Ladkrabang (KMUTL), Bangkok 10520, Thailand
e-mail: kpewisan@gmail.com

T. Tangcharoen · W. Klysubun
Synchrotron Light Research Institute (SLRI), Nakhon
Ratchasima 30000, Thailand

A. Ruangphanit
Thai Microelectronics Center (TMEC), Chachoengsao 24000,
Thailand

W. Pecharapa
Thailand and Center of Excellence in Physics (ThEP Center),
CHE, 328 SiAyutthaya Rd., Bangkok 10400, Thailand

There are many attempts to synthesize nanocrystalline ferrites by various techniques such as chemical co-precipitation process, mechanical alloying, hydrothermal method, microwave hydrothermal synthesis, sol-gel method, microwave-assisted combustion and reverse micelle technique [5, 9, 17–21]. Chemical co-precipitation gives very small particle and symmetric shape but this technique not suitable for large-scale product [22]. Mechanical alloying is allowed to synthesize a lot of product but it is somewhat time consuming process [8, 17]. Hydrothermal and microwave hydrothermal synthesis generally provide high performance but use advanced instrument [23]. Sol-gel method is a simple technique but take rather long time [24]. Among those complicated means, there is a rather simple technique called sol-gel auto-combustion which has considerable advantages such as simple procedure, rapidity, cheap precursors, low external power use and high purity products [4, 25]. This method has been employed to synthesize various kinds of materials such as ferrites, conductive oxide nanoparticles, composites, electrolyte for solid oxide fuel cells, cathode material for batteries and photocatalyst [26–31]. There have been recently a number of reports focusing on the combustion synthesis of NiZn ferrite by using urea, citric acid, glycine and tartaric acid as the fuel [13, 32–34]. Diethanolamine (DEA) is an organic compound with the chemical formula $C_4H_{11}NO_2$. It is both the solid and liquid state which is very soluble in water and ethanol with colorless and a mild ammonia odor. Diethanolamine is inexpensive and widely used as the solvent, adhesive, dispersant, surfactant, corrosion inhibitor and emulsifiers in the petroleum, natural gas, lubricant, textile, paint, paper, agriculture, cosmetics, soap and shampoo manufacturing. Moreover, it is the essential substance for thin films preparation to improve clarity, stability and homogeneity. In terms of thermochemistry, diethanolamine is one of the potential fuels because of its greater heat of combustion comparing to other conventional fuel. The heat of combustion of DEA is -6.00 kcal/g meanwhile the favored fuels such as citric acid, urea or glycine are only -2.76 , -2.98 and -3.24 kcal/g, respectively [35–37]. Based on this propose, our main goal in this work is to utilize DEA as a substitutional fuel for synthesizing Ni-substituted Zn ferrites by sol-gel auto-combustion method with basic device and simple procedure that can reduce the synthesized time and remain the spinel structure characteristics.

2 Experimental

2.1 Materials

Nickel (II) nitrate hexahydrate $[Ni(NO_3)_2 \cdot 6H_2O]$ (≥ 99 %, BDH), zinc (II) nitrate hexahydrate $[Zn(NO_3)_2 \cdot 6H_2O]$

(98 %, Ajax) and iron (III) nitrate nonahydrate $(Fe(NO_3)_3 \cdot 9H_2O)$ (98 %, Ajax) were used as starting materials. Absolute ethanol (C_2H_5OH) (99.9 %, RCI) were used as the solvent and polyvinyl alcohol $[(C_2H_4O)_n]$, PVA] (89 %, Sigma-Aldrich) were used as a binder. Diethanolamine $[(HOCH_2CH_2)_2NH]$, DEA] (≥ 96 %, Fluka) was selected as the fuel. All chemicals in the study were analytical reagent grade and used without further purification.

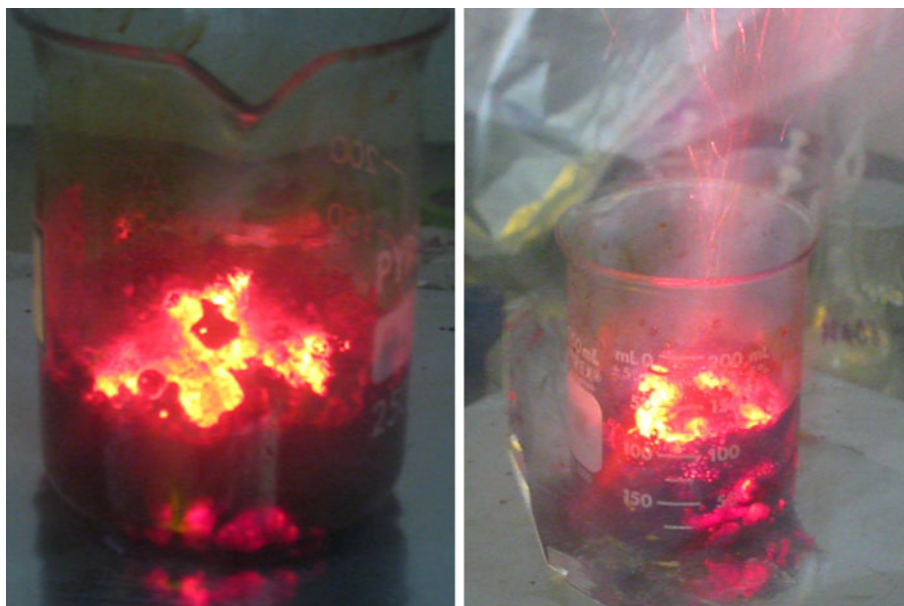
2.2 Preparation of Ni-substituted Zn ferrites

For the synthesis of nanocrystalline Ni-substituted Zn ferrites with compositions of $Ni_xZn_{1-x}Fe_2O_4$, stoichiometric quantities of metal nitrates were dissolved in absolute ethanol to form 0.25 M precursor solution. The solution was prepared with various Ni composition ($x = 0.0$ – 1.0). DEA was added as the fuel into a solution with the equivalence ratio (Φ_c) of the redox mixture. The mixed solution was vigorously stirred at 200 °C using a magnetic stirrer. After 40 min, the mixture obviously changed into a viscous gel and auto-combusted for 5 s until dark-brown powders were obtained (Fig. 1). The obtained product was completely dry therefore it was not necessary to heat in an oven to remove the moisture which is required for regular sol-gel method [38]. A portion of as-synthesized powders were granulated using PVA as a binder and were uniaxial pressed at a pressure of 3 ton/cm² to form pellets. After that, both of as-synthesized powders and green body pellets were gradually heated to 550 °C for 1 h at the rate of about 10 °C/min to remove the binder materials. Finally, the temperature was raised to sintering temperature of $1,000$ °C and kept at this temperature for 4 h.

2.3 Characterizations

The crystal structure and phase identification of sintered ferrite ceramic samples was performed by X-ray diffraction (XRD, PANalytical X'Pert PRO MPD model pw 3040/60) using CuK_α irradiation ($\lambda = 1.54$ Å) in the 2θ range of 20° to 80° at a scanning rate of 0.04° s⁻¹. The chemical properties of after-calcined ferrite powders were investigated by Fourier transform infrared spectroscopy (FTIR) at the range of 400 – 800 cm⁻¹ in the transmittance mode. The microstructures and morphologies of this compound were observed by scanning electron microscope (SEM, JEOL JEM-6510) and field-emission scanning electron microscope (FE-SEM, Hitachi S-4700) operated at an acceleration voltage of 20 kV. The magnetic properties of sintered ceramic samples were examined at a room temperature using the vibrating sample magnetometer (VSM) in an operating range of ± 8 kOe. The specific surface areas were measured and calculated according to the Brunauer–Emmett–Teller (BET) method. The optical absorption spectra were

Fig. 1 The auto-combustion of NiZn ferrite



carried out by the UV–vis spectrophotometer to determine the band gap of ferrites.

2.4 Photocatalytic activity of Ni-substituted Zn ferrites and RhB degradation experiments

The photocatalytic activities of the ferrites were studied by the degradation of Rhodamine B (RhB) under daylight-irradiation. Ni-substituted Zn ferrite ceramic pellet with difference of nickel concentration was put into a glass bottle which contains 25 ml of Rhodamine B solution. The weight of each of ceramic pellet is approximately 0.4 g and the initial concentration of Rhodamine B solution is 3 $\mu\text{mol/L}$. Then, those bottles were placed out of doors under daylight-irradiation without any stirring. After approximately 3 h, each ferrite pellet was taken out from the bottles and the absorption of each RhB solution was measured by the UV–vis spectrophotometer (Thermo Electron Helios Gamma) to investigate the RhB concentration in the remaining solutions. After that, the specific concentration of Ni-substituted Zn ferrite ceramic pellet which give the best degradation of RhB result was selected for further RhB degradation experiment by time variation. The specific ferrite pellet was put into a glass bottle which contained 25 ml of RhB solution with initial concentration of 2 $\mu\text{mol/L}$ and laid down under the daylight-irradiation without any stirring from 0 to 5 h. Finally, the concentrations of remaining RhB in each time-varying solution were determined with the UV–vis spectrophotometer in the wavelength 450–650 nm. The degradation percentage was calculated from the decrease of maximum absorption peak of RhB solution at 552–553 nm.

3 Results and discussion

3.1 The features of Ni-substituted Zn ferrites

The photographs of Ni-substituted Zn ferrites are shown in Fig. 2. It can be observed that the after-calcined powders (Fig. 2b) were distinctly visible in more fine-grained feature than as-synthesized powders (Fig. 2a). After the press and sintering, the sintered ferrite ceramic samples (Fig. 2c) show the compact appearance with smooth surface. In addition, it is noticed that the color of as-synthesized powders, after-calcined powders and sintered ceramic samples are darker with increasing nickel composition.

3.2 X-ray diffraction analysis

Figure 3 shows the X-ray diffraction patterns of ceramic ferrite $\text{Ni}_x\text{Zn}_{1-x}\text{Fe}_2\text{O}_4$ ($x = 0\text{--}1.0$) sintered at 1,000 $^\circ\text{C}$ for 4 h. It is evidently noticed that there are not any strange diffraction peaks such as NiO, ZnO or Fe_2O_3 in all samples but merely the existence of main peaks at 30.2 $^\circ$, 35.5 $^\circ$, 37.1 $^\circ$, 43.1 $^\circ$, 53.4 $^\circ$, 56.9 $^\circ$, 62.4 $^\circ$, 70.8 $^\circ$, 73.8 $^\circ$ and 78.9 $^\circ$, which attribute to the (220), (311), (222), (400), (422), (511), (440), (620), (533) and (444) planes, respectively. These features ensure the formation of NiZn ferrite with single phase spinel cubic crystal structure, which is consistent with previous works [4, 19, 20, 39]. As Ni content increases, the X-ray diffraction patterns noticeably show slight shift in peak position due to the presence of Ni that may cause the formation of a solid solution in the ferrites. In addition, the sharp and intense diffraction peaks indicate that as-synthesized ferrite powders have good crystallinity.

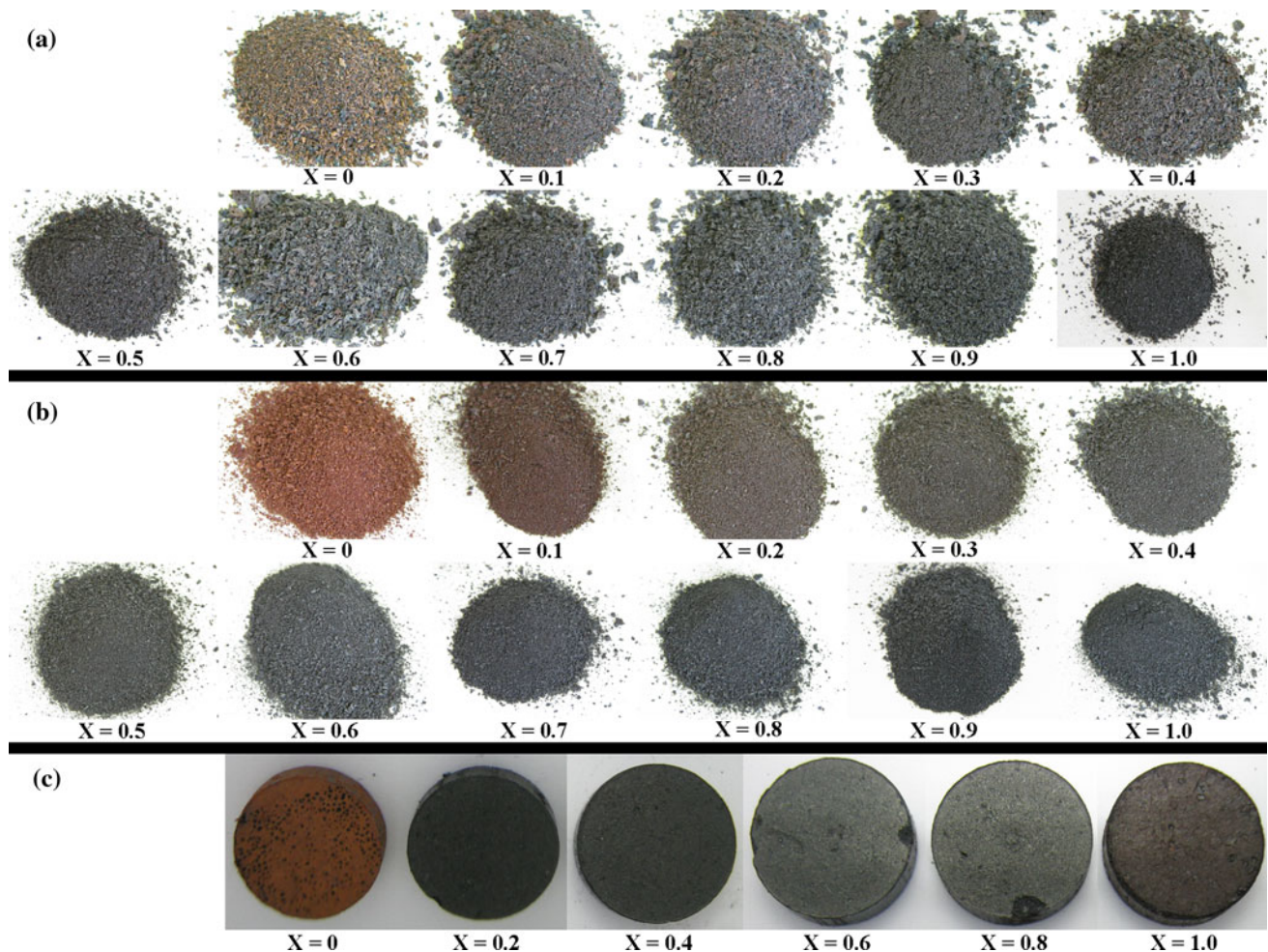


Fig. 2 Photographs of **a** as-synthesized $\text{Ni}_x\text{Zn}_{1-x}\text{Fe}_2\text{O}_4$ powders, **b** after-calcined $\text{Ni}_x\text{Zn}_{1-x}\text{Fe}_2\text{O}_4$ powders and **c** $\text{Ni}_x\text{Zn}_{1-x}\text{Fe}_2\text{O}_4$ sintered ceramic samples

The crystallite size (D) of each composition for after-calcined ferrite samples was calculated from the full width at half-maximum (FWHM) of the strongest diffraction peak (311) using the Scherrer's equation (1), where D is crystallite size, λ is wavelength of X-ray source ($\text{CuK}_\alpha = 1.54 \text{ \AA}$), β is FWHM of the (311) diffraction peak and θ is the position of diffraction angle. In addition, interplanar distance (d), lattice parameter (a) and x-ray density ($\rho_{x\text{-ray}}$) of after-calcined ferrite samples were evaluated by Eqs. (2), (3) and (4), respectively. (hkl) is Miller plane, M is the molecular weight of each samples and N is Avogadro's constant ($6.022 \times 10^{23} \text{ mol}^{-1}$). All of the calculated results are listed in the Table 1.

$$D = \frac{0.9\lambda}{\beta \cos \theta} \quad (1)$$

$$d_{hkl} = \frac{\lambda}{2 \sin \theta} \quad (2)$$

$$a = d_{hkl} (h^2 + k^2 + l^2)^{\frac{1}{2}} \quad (3)$$

$$\rho_{x\text{-ray}} = \frac{8M}{Na^3} \quad (4)$$

From Table 1, the smallest crystallite size (D) is found in $\text{Ni}_{0.5}\text{Zn}_{0.5}\text{Fe}_2\text{O}_4$ powders and the average crystallite size of all samples is approximately 40 nm. The interplanar distance and lattice parameter tend to decrease with increasing of nickel concentration meanwhile the X-ray density has the discontinuous values. These calculation results are in concordance to the other work [22, 34]. When the ferrite was doped with Ni^{2+} ion, its lattice parameter slightly decreases from 8.370 to 8.292 \AA . This result is comprehensively considered that the replacement of larger Zn^{2+} (0.74 \AA) ion by Fe^{3+} ions with smaller ionic radius of 0.64 \AA at tetrahedral sites. Those Fe^{3+} ions are pushed from the octahedral sites by the incremental Ni^{2+} ions,

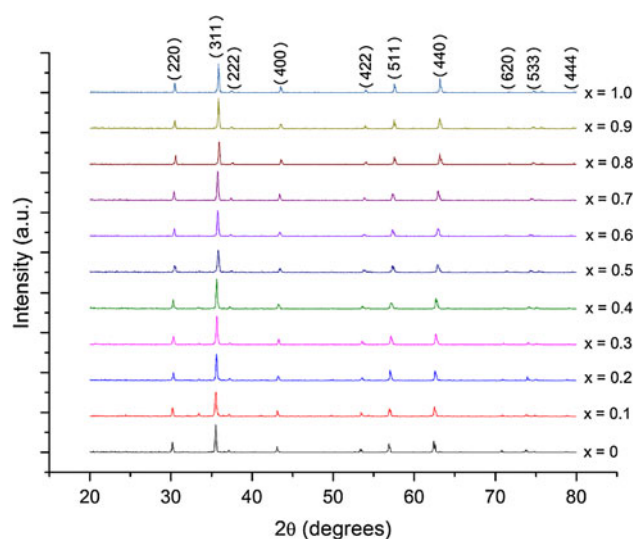


Fig. 3 XRD patterns of $\text{Ni}_x\text{Zn}_{1-x}\text{Fe}_2\text{O}_4$ sintered ceramic samples

Table 1 Crystallite size (D), interplanar distance (d), lattice parameter (a) and X-ray density ($\rho_{x\text{-ray}}$) of the $\text{Ni}_x\text{Zn}_{1-x}\text{Fe}_2\text{O}_4$ sintered ceramic samples

Compound	x	D (nm)	d (Å)	a (Å)	$\rho_{x\text{-ray}}$ (g/cm ³)
ZnFe_2O_4	0	42.41	2.524	8.370	5.462
$\text{Ni}_{0.1}\text{Zn}_{0.9}\text{Fe}_2\text{O}_4$	0.1	37.32	2.523	8.369	5.449
$\text{Ni}_{0.2}\text{Zn}_{0.8}\text{Fe}_2\text{O}_4$	0.2	41.77	2.517	8.348	5.476
$\text{Ni}_{0.3}\text{Zn}_{0.7}\text{Fe}_2\text{O}_4$	0.3	39.34	2.514	8.338	5.478
$\text{Ni}_{0.4}\text{Zn}_{0.6}\text{Fe}_2\text{O}_4$	0.4	40.14	2.516	8.344	5.451
$\text{Ni}_{0.5}\text{Zn}_{0.5}\text{Fe}_2\text{O}_4$	0.5	34.54	2.503	8.302	5.520
$\text{Ni}_{0.6}\text{Zn}_{0.4}\text{Fe}_2\text{O}_4$	0.6	39.49	2.507	8.313	5.481
$\text{Ni}_{0.7}\text{Zn}_{0.3}\text{Fe}_2\text{O}_4$	0.7	40.56	2.507	8.315	5.462
$\text{Ni}_{0.8}\text{Zn}_{0.2}\text{Fe}_2\text{O}_4$	0.8	42.20	2.495	8.275	5.527
$\text{Ni}_{0.9}\text{Zn}_{0.1}\text{Fe}_2\text{O}_4$	0.9	43.31	2.501	8.293	5.475
NiFe_2O_4	1.0	42.56	2.500	8.292	5.461

reflecting the increase in Ni substitution content consequently results to lattice shrinkage [40].

3.3 FT-IR analysis

In order to confirm the constitution of the spinel structure and to understand the chemical characteristics of ferrite, the Fourier transform infrared (FTIR) spectroscopy of after-calcined Ni-substituted Zn ferrite powders were performed in the wavenumber range 400–800 cm^{-1} in transmittance mode at room temperature. The results from FTIR measurement for the after-calcined $\text{Ni}_x\text{Zn}_{1-x}\text{Fe}_2\text{O}_4$ ($x = 0, 0.5$ and 1.0) powders are exhibited in Fig. 4. For all ferrite materials, there are two main absorption bands in the 400 and 550 cm^{-1} range which are attributable to the formation of the spinel phase [8, 41]. A noticeable absorption band at

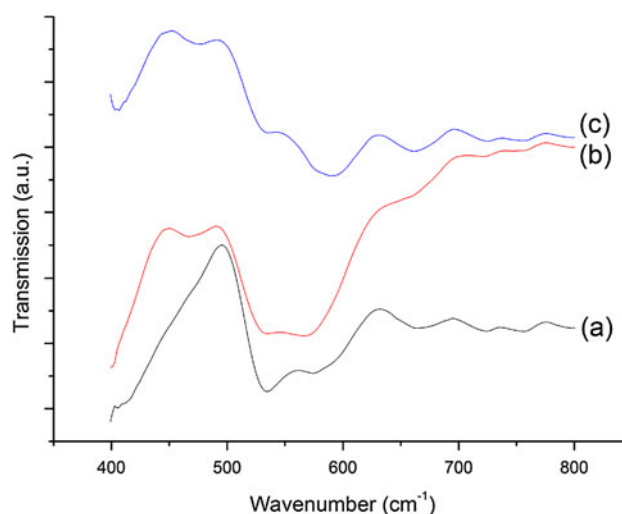
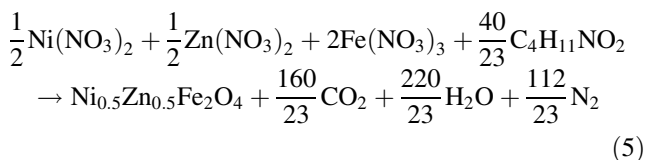


Fig. 4 FTIR spectra of after-calcined (a) ZnFe_2O_4 , (b) $\text{Ni}_{0.5}\text{Zn}_{0.5}\text{Fe}_2\text{O}_4$ and (c) NiFe_2O_4 powders

about 400–450 cm^{-1} ascribes to the stretch mode of $\text{Fe}^{3+}-\text{O}^{2-}$ in the octahedral sites. The intensity of this band decreases when the Ni^{2+} ions are added into the spinel structure (Fig. 4c). This effect can be explained from the fact that the increasing Ni^{2+} ions could replace some of Fe^{3+} ions in the octahedral sites and push them to tetrahedral sites, leading to significant change in the absorption efficiency [42]. Moreover, the increment of nickel concentration caused the appearance of a new band located at 470 cm^{-1} in both of $\text{Ni}_{0.5}\text{Zn}_{0.5}\text{Fe}_2\text{O}_4$ (Fig. 4b) and NiFe_2O_4 (Fig. 4c) ferrite [43]. The next absorption band situated between 530 and 580 cm^{-1} corresponds to the stretching vibration of $\text{Fe}^{3+}-\text{O}^{2-}$ and $\text{Zn}^{2+}-\text{O}^{2-}$ in the tetrahedral sites. When Zn ferrites are doped with Ni, the absorption band at around 580 cm^{-1} increases due to some Fe^{3+} ions are pushed by the additional Ni^{2+} ions in the octahedral sites and accumulate with the original Fe^{3+} ions in the tetrahedral resulting to the elevated absorption efficiency. On the other hand, the decrease of absorption band at about 530 cm^{-1} may be explained that Zn^{2+} ions in the tetrahedral sites are subsided and bear upon the absorption efficiency [44]. In addition, comparing with Zn ferrite sample, it is observable that the wave number of all Ni-doped ferrite samples noticeably shifts to higher value. This occurrence may arise from the fact that Ni has greater ionic radius (0.69 Å) than Fe^{3+} ion (0.64 Å). As Ni concentration increases, it is able to drive Fe^{3+} ion to tetrahedral site. Moreover, the length of Fe–O bond will change and bear upon the absorption efficiency [34]. Furthermore, the existence of additional absorption bands is noticeable at around 650–800 cm^{-1} , which are identified as the vibrations of some inorganic compound. This contaminant may originate from the incomplete reaction during combustion process.

3.4 Thermodynamics of combustion synthesis

The Ni-substituted Zn ferrite is produced by the auto-combustion route using the thermochemical decomposition of the nitrate mixture. Nickel (II) nitrate hexahydrate, zinc (II) nitrate hexahydrate and iron (III) nitrate nonahydrate were used as the source of Ni, Zn and Fe, respectively. During heating, DEA can play a crucial role as abundant carbon (C) source and mix with nitrogen (N) to form the flash combustion gas for self-ignited process. Due to comparably great heat of combustion, DEA can efficiently provide sufficient thermal energies to the system and initiate the reaction and crystallization processes with reducing time. The complete chemical reaction for the synthesis of $\text{Ni}_x\text{Zn}_{1-x}\text{Fe}_2\text{O}_4$ powders (for example $x = 0.5$) with DEA could be possibly written in the following equation:



For the maximum combustion efficiency, the total oxidizing and reducing valencies of the oxidizer (O) and the fuel (F) should be balanced which is represented in term of the oxidizer-to-fuel ratio ($\Phi_e = 1$). In this work, all metal nitrates [$\text{M}(\text{NO}_3)_2$, $\text{M} = \text{Ni}, \text{Zn}$] and iron (III) nitrate [$\text{Fe}(\text{NO}_3)_3$] act as oxidizers in ferrite (MFe_2O_4) meanwhile diethanolamine [$(\text{HOCH}_2\text{CH}_2)_2\text{NH}$] acts as a fuel. In addition, the oxidizing and reducing valencies of C, H, O, N, Fe and M are -4 , -1 , 2 , 0 , -3 and -2 , respectively [45].

$$\Phi_e = \frac{(\text{n}) \text{ total valencies of fuel}}{\text{total valencies of oxidizer}}$$

$$1 = \frac{(\text{n})[(4\text{C} \times -4) + (1\text{N} \times 0) + (11\text{H} \times -1) + (2\text{O} \times 2)]}{[(1\text{M} \times -2) + (2\text{N} \times 0) + (6\text{O} \times 2)] + [(2\text{Fe} \times -3) + (6\text{N} \times 0) + (18\text{O} \times 2)]}$$

$$\text{n} = \frac{40}{23} = 1.74$$

Thus, the molar ratio of metal nitrates and fuel ($\text{M}^{2+}:\text{Fe}^{3+}:\text{DEA}$) is 1:2:1.74 which provides the adequate heat for the maximum combustion process.

3.5 SEM analysis

The morphological characteristics and the microstructures of after-calcined Ni-substituted Zn ferrite powders with

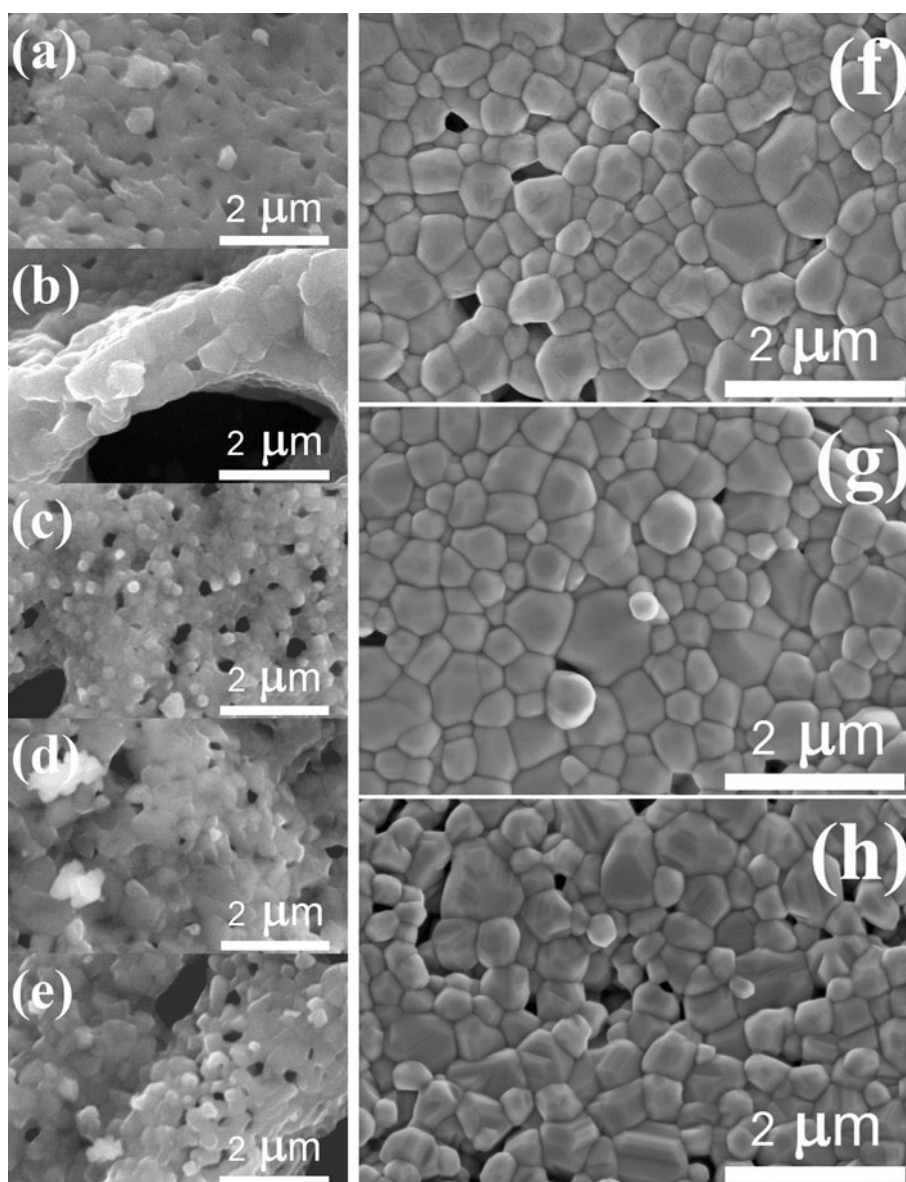
various nickel content ($x = 0, 0.2, 0.5, 0.8$ and 1.0) are shown by SEM images in Fig. 5a–e. After the calcinations, it is clearly seen that the ferrite powders possess finer uniform particle size with homogenous spherical shape and big pores. Even though the crystallite size of after-calcined powders are in the nano range, but the magneto-dipole interactions between the particles and the calcination at high temperature can consequently result the agglomeration and generate the secondary phase cluster that made their size greater than the estimated values from the X-ray diffraction data [46]. Moreover, it is noticed that the particle size of ferrite powders slightly increases when the nickel concentration increases [47]. Figure 5f–h shows the high magnified SEM photographs of after-calcined $\text{Ni}_x\text{Zn}_{1-x}\text{Fe}_2\text{O}_4$ ($x = 0.6, 0.8$ and 1.0) sintered ceramic samples. The noticeable change in their grain size is observed as the nickel composition increases. The average grain size of all samples is approximately $0.4 \mu\text{m}$ which slightly decreases when nickel concentration increases. In addition, the microstructures of Ni-substituted Zn ferrites show loose structure with more pores (Fig. 5h) [48].

3.6 VSM analysis

The variation of magnetic hysteresis loop for all compositions of $\text{Ni}_x\text{Zn}_{1-x}\text{Fe}_2\text{O}_4$ ($x = 0, 0.2, 0.4, 0.6, 0.8$ and 1.0) sintered ceramic samples were investigated by vibrating sample magnetometer (VSM) operated at room temperature with an applied field of $\pm 8 \text{ kOe}$ and the corresponding results are shown in Fig. 6. All of magnetization curves show a normal S-shape type which is a typical ferrimagnetism characteristic [49]. It is observed that the

magnetization increases as the nickel content increases up to $x = 0.8$ thereafter decreases with further increase in nickel composition up to $x = 1.0$. The plot of saturation magnetization (M_s) versus concentration of nickel shown in Fig. 7 indicates that the saturation magnetization increases sharply with the increasing x and reaches the maximum of 100.3 emu/g when x is 0.8 and then decreases to 69.7 emu/g as x is 1.0 . Moreover, Fig. 7 illustrates an

Fig. 5 SEM photographs of after-calcined **a** ZnFe_2O_4 , **b** $\text{Ni}_{0.2}\text{Zn}_{0.8}\text{Fe}_2\text{O}_4$, **c** $\text{Ni}_{0.5}\text{Zn}_{0.5}\text{Fe}_2\text{O}_4$, **d** $\text{Ni}_{0.8}\text{Zn}_{0.2}\text{Fe}_2\text{O}_4$ and **e** NiFe_2O_4 powders with FE-SEM photographs of **f** $\text{Ni}_{0.6}\text{Zn}_{0.4}\text{Fe}_2\text{O}_4$, **g** $\text{Ni}_{0.8}\text{Zn}_{0.2}\text{Fe}_2\text{O}_4$, **h** NiFe_2O_4 sintered ceramic samples



increase in the coercivity from 0 to 91.8 Oe with increasing Ni concentration while the maximum value of the coercivity is found for x is 1.0. The increase in saturation magnetization with increasing Ni content can be physically explained. When loading Ni content increases, Ni^{2+} ions can effectively occupy octahedral (B) sites and some Fe^{3+} ions have a tendency to go into the tetrahedral (A) sites and replace the Zn^{2+} ions which has no magnetic moment. Every step of Ni^{2+} substitution, an equal amount of Fe^{3+} ions (5 Bohr magneton) from the B sites would increasingly transfer to replace the Zn^{2+} ion sites. This result consequently leads to the unequal of the magnetic moment of Fe^{3+} ions at A and B sites and generates the net magnetic moment. In addition, each increasing of substituted Ni^{2+} ions (2 Bohr magneton) would provide the net magnetic moment from itself [34, 40]. In case of Zn ferrite

(ZnFe_2O_4), there are 8 Zn^{2+} ions, 16 Fe^{3+} ions and 32 O^{2-} ions in each unit cell. Because oxygen ions are the neutral ion in magnetism, they have not any effect to the magnetic properties of ferrite. Owing to Zn ferrite has the normal spinel structure, the 8 Zn^{2+} ions are occupied all of 8 points in tetrahedral sites and 16 Fe^{3+} ions are occupied all of 16 points in octahedral sites but each half of them have spin in the opposite direction. For Zn^{2+} ions, there has not any unpaired electron (or Bohr magneton) which generates the magnetic moment and the magnetic moments generated from Fe^{3+} ions normally contradict each other, resulting to the disappearance of total Bohr magneton in each unit cell of ZnFe_2O_4 . Meanwhile, in case of $\text{Ni}_{0.8}\text{Zn}_{0.2}\text{Fe}_2\text{O}_4$, there are 6 Ni^{2+} ions, 2 Zn^{2+} ions and 16 Fe^{3+} ions in each unit cell. It has an inverse spinel structure which 8 points in tetrahedral sites are occupied by 2 Zn^{2+} ions and 6 Fe^{3+}

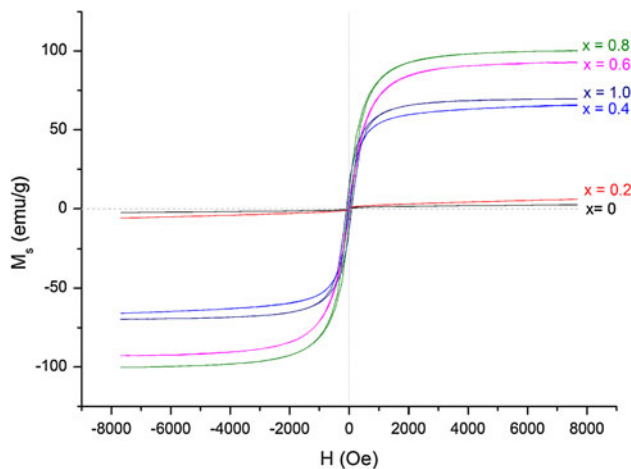


Fig. 6 Magnetization behavior of $\text{Ni}_x\text{Zn}_{1-x}\text{Fe}_2\text{O}_4$ sintered ceramic samples at room temperature

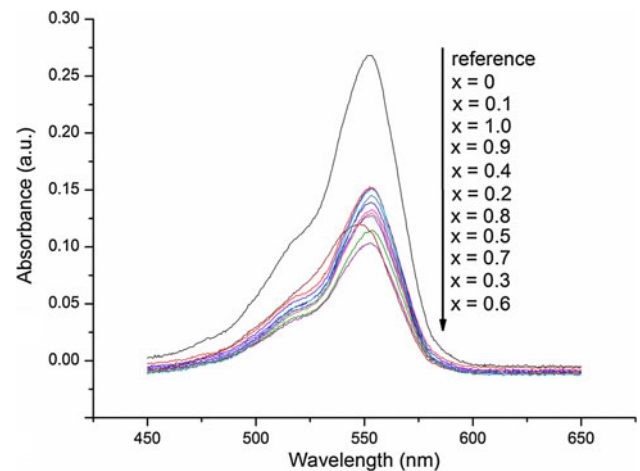


Fig. 8 The UV-Vis absorption spectra for RhB solution (3 $\mu\text{mol/L}$) in the presence of $\text{Ni}_x\text{Zn}_{1-x}\text{Fe}_2\text{O}_4$ sintered ceramic samples under daylight-irradiation for 3 h

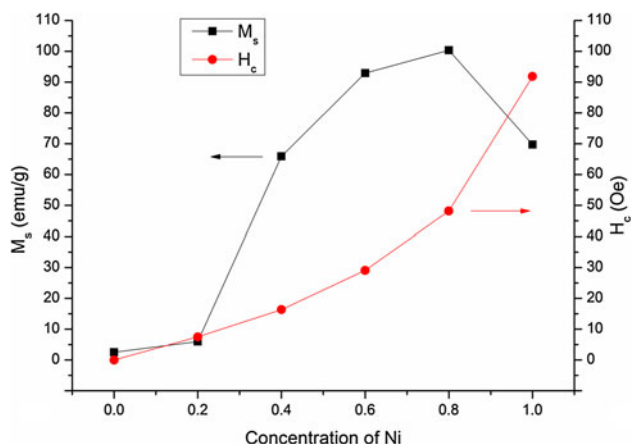


Fig. 7 Dependence of the saturation magnetization and coercivity of after-calcined $\text{Ni}_x\text{Zn}_{1-x}\text{Fe}_2\text{O}_4$ sintered ceramic samples with x values

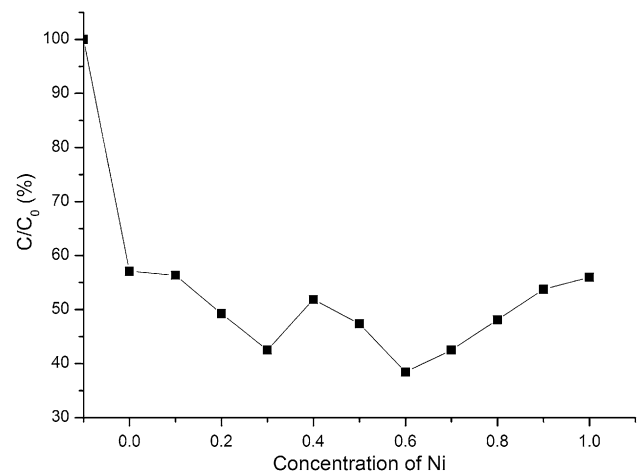


Fig. 9 Photodegradation of RhB solution (3 $\mu\text{mol/L}$) in the presence of $\text{Ni}_x\text{Zn}_{1-x}\text{Fe}_2\text{O}_4$ sintered ceramic samples under daylight-irradiation for 3 h as the normalized concentration change versus nickel concentration

ions. The remain of 10 Fe^{3+} ions and 6 Ni^{2+} ions generally occupy 16 points of octahedral sites. The net magnetic moment are generated from the 4 Fe^{3+} ions (each ions have 5 Bohr magneton) accompanying the magnetic moment of 6 Ni^{2+} ions (each ions have 2 Bohr magneton). Therefore, total Bohr magneton in each unit cell for $\text{Ni}_{0.8}\text{Zn}_{0.2}\text{Fe}_2\text{O}_4$ is 32 Bohr magneton. Thus, the $\text{Ni}_{0.8}\text{Zn}_{0.2}\text{Fe}_2\text{O}_4$ will have the higher net magnetization. However, when the nickel ions substitute all zinc ions, in case of NiFe_2O_4 , there are 8 Ni^{2+} ions and 16 Fe^{3+} ions in each unit cell. With general inverse spinel structure, there are 8 points in tetrahedral sites occupied by 8 Fe^{3+} ions and the remaining 8 Fe^{3+} ions and 8 Ni^{2+} ions would occupy 16 points of octahedral sites. The Fe^{3+} ions in each lattice sites with opposite spin direction would contradict each other. As a result, the net Bohr magneton in each unit cell for NiFe_2O_4 , which is

resulted merely from the total magnetic moment of 8 Ni^{2+} ions is 16 Bohr magneton. This primary explanation could be the suitable reason that $\text{Ni}_{0.8}\text{Zn}_{0.2}\text{Fe}_2\text{O}_4$ typically has higher magnetization than Ni ferrite (NiFe_2O_4) [1, 2, 49, 50]. Moreover, the maximum coercive force for Ni-doped Zn ferrites is 91.8 Oe which is found in Ni ferrite (NiFe_2O_4). It is presumably due to the alternation of particle and grain size of ferrite sample generated before and after the nickel doping. Comparing to $\text{Ni}_{0.6}\text{Zn}_{0.4}\text{Fe}_2\text{O}_4$ and $\text{Ni}_{0.8}\text{Zn}_{0.2}\text{Fe}_2\text{O}_4$ (Fig. 5f, g), the smaller particle size and grain size of Ni ferrite (Fig. 5h) could have lower magnetic domains and domain walls, resulting to the higher energy consumption which is external magnetic field for demagnetization [51, 52].

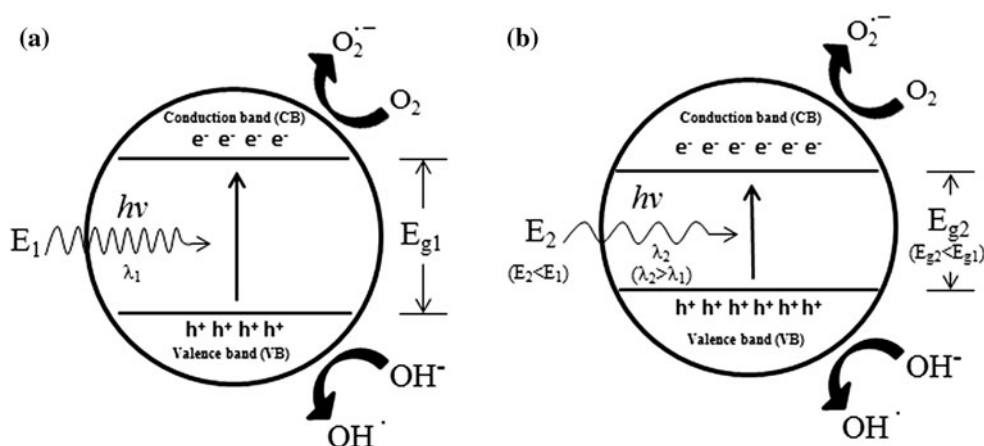


Fig. 10 Schematic of possible mechanism of **a** Zn ferrite and **b** Ni-doped Zn ferrite to produce OH^{\cdot} and $O_2^{\cdot-}$ for react with the contaminants

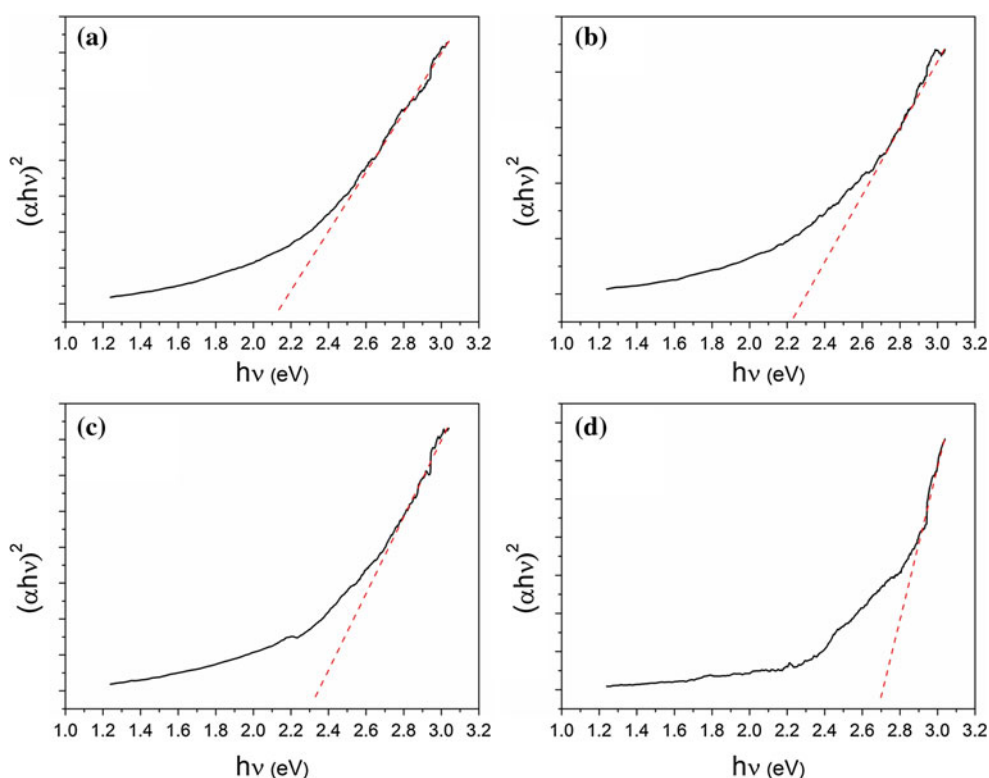


Fig. 11 Plots of $(\alpha h\nu)^2$ versus $h\nu$ of **a** $Ni_{0.6}Zn_{0.4}Fe_2O_4$, **b** $Ni_{0.7}Zn_{0.3}Fe_2O_4$, **c** $Ni_{0.9}Zn_{0.1}Fe_2O_4$ and **d** $NiFe_2O_4$ powders

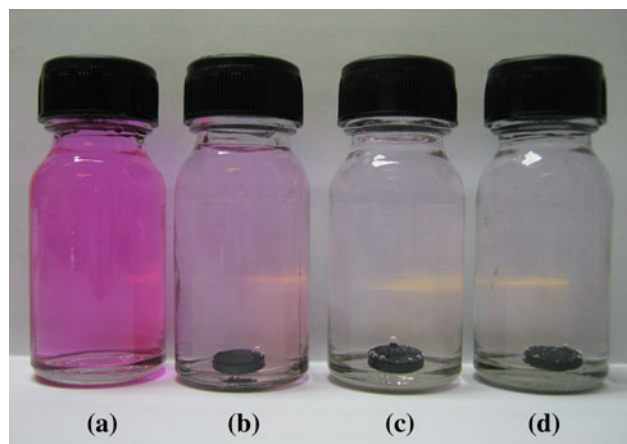
3.7 Photocatalytic activity

Figure 8 shows the change in the absorption spectra of RhB solution after degradation with the $Ni_xZn_{1-x}Fe_2O_4$ ($x = 0-1.0$) sintered ceramic samples under the daylight-irradiation for 3 h without any stirring. It is found that there is the strongest absorbance peak of RhB solution at 553 nm which reduces rapidly [53]. It can be seen that the removal performance initially increases with increasing nickel

composition and continually decreases with the exorbitant nickel concentration (Fig. 9). The great removal efficiency for RhB with nearly 62 % was performed by the sample with nickel concentration of 0.6. There are two possible reasons responsible for this feature. It can be noticed from Table 1 that, the group of smaller crystallite size is found in $Ni_{0.3}Zn_{0.7}Fe_2O_4$, $Ni_{0.5}Zn_{0.5}Fe_2O_4$ and $Ni_{0.6}Zn_{0.4}Fe_2O_4$. This group exhibited better degradation efficiency comparing to the larger crystal size group such as $ZnFe_2O_4$

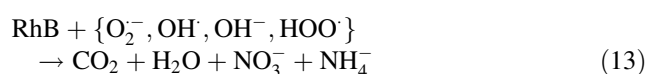
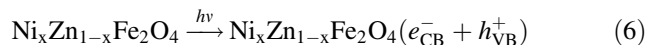
Table 2 Specific surface area (S_{BET}) of the $\text{Ni}_x\text{Zn}_{1-x}\text{Fe}_2\text{O}_4$ powders

Compound	x	S_{BET} (m^2g^{-1})
ZnFe_2O_4	0	0.91
$\text{Ni}_{0.5}\text{Zn}_{0.5}\text{Fe}_2\text{O}_4$	0.5	1.11
$\text{Ni}_{0.6}\text{Zn}_{0.4}\text{Fe}_2\text{O}_4$	0.6	3.25
NiFe_2O_4	1.0	0.79

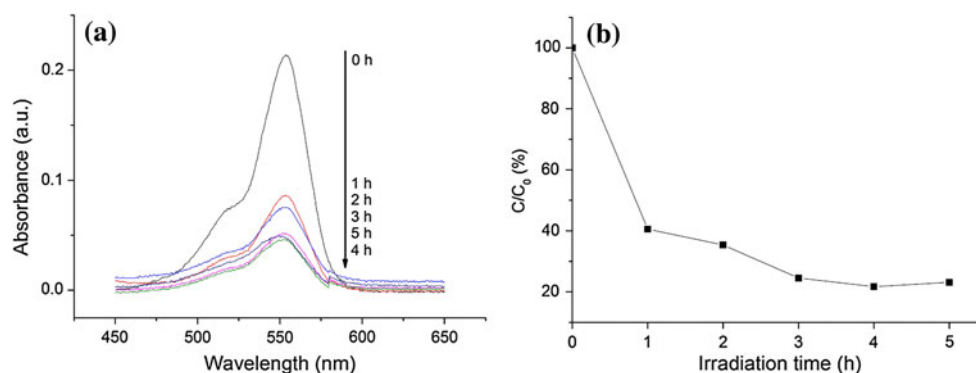
**Fig. 12** The photograph of RhB solution (3 $\mu\text{mol/L}$) in the presence of **a** reference, **b** $\text{Ni}_{0.1}\text{Zn}_{0.9}\text{Fe}_2\text{O}_4$, **c** $\text{Ni}_{0.6}\text{Zn}_{0.4}\text{Fe}_2\text{O}_4$ and **d** $\text{Ni}_{0.8}\text{Zn}_{0.2}\text{Fe}_2\text{O}_4$ sintered ceramic samples after 3 h of daylight-irradiation

(42.41 nm), $\text{Ni}_{0.9}\text{Zn}_{0.1}\text{Fe}_2\text{O}_4$ (43.31 nm) and NiFe_2O_4 (42.56 nm). Increasing surface areas of the samples due to reduction in particle size can provide greater active surface area, leading to the enhancement of photocatalytic efficiency [54]. Second reason could be attributable to the energy gaps of the ferrites. The energy gap of photocatalyst material typically determines the wavelength of light that can be absorbed leading to the generation of the electron–hole pairs which will react with water molecule, hydroxide ions and oxygen molecule to form hydroxyl radicals (OH^\cdot and OH^-) and active oxygen species ($\text{O}_2^{\cdot-}$ and HOO^\cdot) as depicted in Fig. 10a. Both hydroxyl radicals and active oxygen species will hold and react with the organic

compound to perform the complete oxidation process and make those contaminants unceasingly degenerated [54]. The possible mechanism of photocatalysis for $\text{Ni}_x\text{Zn}_{1-x}\text{Fe}_2\text{O}_4$ under daylight irradiation can be described by the following equations [55]:



The alteration in energy gap of ferrites has an effect on the daylight absorption efficiency (Fig. 10b). The lower energy gap can absorb higher wavelength spectrum which mainly found in the solar spectrum that reach the earth's surface. Thus, the low energy gap ferrites can easily generate more electron–hole pairs with less time and contribute to the better degradation efficiency. It was reported that the energy gap of some ferrite such as NiFe_2O_4 , ZnFe_2O_4 and $\text{Ni}_{0.5}\text{Zn}_{0.5}\text{Fe}_2\text{O}_4$ were found to be 2.19, 1.92 and 1.87 eV, respectively [54, 56] with corresponding wavelength in middle sunlight up to 663 nm, resulting an effectiveness of these ferrites under sunlight. From those unequal results, it might be concluded that the energy gap of $\text{Ni}_x\text{Zn}_{1-x}\text{Fe}_2\text{O}_4$ depends on the ratio between Ni ions and Zn ions in each ferrite composition. Figure 11 exhibits the band gaps of the ferrites which were calculated from their absorption spectra while Table 2 shows their specific BET surface areas. It can be observed from these additional results that the samples with better degradation ($x = 0.5, 0.6$ and 0.7) have lower band gap with higher surface areas than the others ($x = 0, 0.9$ and 1.0). It is observable from Figs. 9 and 12 that

Fig. 13 **a** The UV–Vis absorption spectra for RhB solution (2 $\mu\text{mol/L}$) in the presence of $\text{Ni}_{0.6}\text{Zn}_{0.4}\text{Fe}_2\text{O}_4$ sintered ceramic samples under daylight-irradiation with differing irradiation time, **b** normalized concentration change versus irradiation time

the photodegradation efficiency noticeably increases with increasing nickel concentration up to $x = 0.6$ thereafter decreases, that may due to the appropriate ratio between Ni ions and Zn ions in the ferrite that has low energy band gap and high active surface area reflecting to the superiority in RhB degradation efficiency. The degradation of RhB by $\text{Ni}_{0.6}\text{Zn}_{0.4}\text{Fe}_2\text{O}_4$ under sunlight as function of reaction time was carried out. The corresponding result in term of its absorption spectra is illustrated in Fig. 13a and the normalized RhB concentration versus illuminated time is shown in Fig. 13b. The photocatalytic activity of this ferrite is effective, accompanying the rapid decrease by 60 % from initial concentration after 1 h of illumination and thereafter gradual decrease. The degradation efficiency for RhB using this ferrite can reaches to 77 % within 4 h of reaction time under sunlight.

4 Conclusions

In this work, nanocrystalline Ni-substituted Zn ferrite sintered ceramic samples with different concentration of nickel were successfully synthesized from metal nitrates by sol–gel auto-combustion method using diethanolamine (DEA) as the fuel. The XRD results disclose the single-phase cubic spinel structure of these ferrites. The calculation from diffraction data revealed that the crystallite size gradually decreased with the increase in Ni substitution when $x \leq 0.5$ and increased when $x > 0.5$ suggesting that the ferrite with general formula $\text{Ni}_{0.5}\text{Zn}_{0.5}\text{Fe}_2\text{O}_4$ had the smallest crystallite size. The FTIR results strongly confirm the existence of spinel phase for this ferrite meanwhile SEM and FE-SEM micrographs present the aspect of both ferrite sintered ceramic samples and after-calcined ferrite powders which are in the form of assemblies of nanoparticles. The saturation magnetization increases with increasing nickel concentration and the maximum value at 100.3 emu/g is reached when nickel concentration is 0.8 but the maximum coercivity of 91.8 Oe is obtained for the ferrite with nickel concentration of 1.0. Moreover, the photocatalytic experiment shows that the best removal performance for Rhodamine B was found in $\text{Ni}_{0.6}\text{Zn}_{0.4}\text{Fe}_2\text{O}_4$ which increases up to 77 % in 4 h. This work acknowledges that the nanocrystalline Ni-substituted Zn ferrites with optimum properties modified by Ni content for multipurposed applications can be synthesized by facile process with the accompaniment of DEA as alternatively potential fuel.

Acknowledgments This work has partially been supported by the Synchrotron Light Research Institute (Public Organization) with the PhD scholarship GS-55-D02 for T. Tangcharoen and the National Nanotechnology Center (NANOTEC), NSTDA, Ministry of Science and Technology, Thailand, through its program of Center of

Excellence Network and Thai Microelectronics Center (TMEC), NSTDA, Ministry of Science and Technology, Thailand. Authors would like to thank KMITL Research Fund, Scientific Instruments Service Centre (SISC) of KMITL for FTIR measurement, Rajamangala University of Technology Thanyaburi (RMUTT) for XRD and SEM measurement, Thai Microelectronics Center (TMEC) for FE-SEM measurement and Department of Physics, Kasetsart University (KU) for VSM measurement.

References

- Goldman A (2006) Crystal structure of ferrites: modern ferrite technology, 2nd edn. Springer Science + Business Media, Inc., New York
- Moulson AJ, Herbert JM (2003) Magnetic ceramics: electroceramics, 2nd edn. Wiley, West Sussex
- Pawar DK, Pawar SM, Patil PS, Kolekar SS (2011) Synthesis of nanocrystalline nickel–zinc ferrite ($\text{Ni}_{0.8}\text{Zn}_{0.2}\text{Fe}_2\text{O}_4$) thin films by chemical bath deposition method. *J Alloy Compd* 509:3587–3591
- Azadmanjiri J (2008) Structural and electromagnetic properties of Ni–Zn ferrites prepared by sol–gel combustion method. *Mater Chem Phys* 109:109–112
- Praveena K, Sadhana K, Bharadwaj S, Murthy SR (2009) Development of nanocrystalline Mn–Zn ferrites for high frequency transformer applications. *J Magn Magn Mater* 321: 2433–2437
- Li L, Peng L, Li Y, Zhu X (2012) Structure and magnetic properties of Co-substituted NiZn ferrite thin films synthesized by the sol–gel process. *J Magn Magn Mater* 324:60–62
- Fan G, Gu Z, Yang L, Li F (2009) Nanocrystalline zinc ferrite photocatalysts formed using the colloid mill and hydrothermal technique. *Chem Eng J* 155:534–541
- Jalaly M, Enayati MH, Karimzadeh F, Kameli P (2009) Mechanochemical synthesis of nanostructured magnetic Ni–Zn ferrite. *Powder Technol* 193:150–153
- Kumar A, Annveer M, Arora MS, Yadav RP (2010) Pant, Induced size effect on Ni doped nickel zinc ferrite nanoparticles. *Phys Proc* 9:20–23
- Petzold J (2003) Applications of nanocrystalline softmagnetic materials for modern electronic devices. *Scripta Mater* 48:895–901
- Li L (2011) Glycol-assisted autocombustion synthesis of spinel ferrite CoFe_2O_4 nanoparticles: magnetic and electrochemical performances. *J Sol–Gel Sci Technol* 58:677–681
- Herzer G, Vazquez M, Knobel M, Zhukov A, Reiningner T, Davies HA, Grossinger R, Sanchez JL (2005) Round table discussion: present and future applications of nanocrystalline magnetic materials. *J Magn Magn Mater* 294:252–266
- Peng CH, Hwang CC, Wan J, Tsai JS, Chen SY (2005) Microwave-absorbing characteristics for the composites of thermal-plastic polyurethane (TPU)-bonded NiZn-ferrites prepared by combustion synthesis method. *Mater Sci Eng, B* 117:27–36
- Aphesteguy JC, Jacobo SE, Schegoleva NN, Kurlyandskaya GV (2010) Characterization of nanosized spinel ferrite powders synthesized by coprecipitation and autocombustion method. *J Alloy Compd* 495:509–512
- Brown P, Hope-Weeks LJ (2009) The synthesis and characterization of zinc ferrite aerogels prepared by epoxide addition. *J Sol–Gel Sci Technol* 51:238–243
- Hou JG, Qu YF, Ma WB, Sun QC (2007) Effect of $\text{CuO-Bi}_2\text{O}_3$ on low temperature sintered MnZn-ferrite by sol–gel auto-combustion method. *J Sol–Gel Sci Technol* 44:15–20
- Ismail I, Hashim M, Matori KA, Alias R, Hassan J (2011) Milling time and BPR dependence on permeability and losses of

- Ni_{0.5}Zn_{0.5}Fe₂O₄ synthesized via mechanical alloying process. *J Magn Magn Mater* 323:1470–1476
18. Wang HW, Kung SC (2004) Crystallization of nanosized Ni–Zn ferrite powders prepared by hydrothermal method. *J Magn Magn Mater* 270:230–236
 19. Prakash I, Nallamuthu N, Muralidharan P, Venkateswarlu M (2011) Manjusri Misra, Amar Mohanty, N. Satyanarayana, Preparation and characterization of nanocrystalline CoFe₂O₄ deposited on SiO₂: in situ sol–gel process. *J Sol–Gel Sci Technol* 58:24–32
 20. Wang Z, Fei W, Qian H, Jin M, Shen H, Jin M, Xu J, Zhang W, Bai Q (2012) Structure and magnetic properties of CoFe₂O₄ ferrites synthesized by sol–gel and microwave calcination. *J Sol–Gel Sci Technol* 61:289–295
 21. Misra RDK, Gubbala S, Kale A, Egelhoff WF Jr (2004) A comparison of the magnetic characteristics of nanocrystalline nickel, zinc, and manganese ferrites synthesized by reverse micelle technique. *Mater Sci Eng, B* 111:164–174
 22. Jadhav S, Shirsath SE, Toksha BG, Shengule DR, Jadhav KM (2008) Structural and dielectric properties of Ni–Zn ferrite nanoparticles prepared by co-precipitation method. *J Optoelectron Adv Mater* 10:2644–2648
 23. Lee JH, Kim CK, Katoh S, Murakami R (2001) Microwave-hydrothermal versus conventional hydrothermal preparation of Ni- and Zn-ferrite powders. *J Alloy Compd* 325:276–280
 24. He X, Song G, Zhu J (2005) Non-stoichiometric NiZn ferrite by sol–gel processing. *Mater Lett* 59:1941–1944
 25. Geng Q, Zhao X, Gao X, Yang S, Liu G (2012) Low-temperature combustion synthesis of CuCr₂O₄ spinel powder for spectrally selective paints. *J Sol–Gel Sci Technol* 61:281–288
 26. Zhang J, Gao L (2004) Synthesis of antimony-doped tin oxide (ATO) nanoparticles by the nitrate–citrate combustion method. *Mater Res Bull* 39:2249–2255
 27. Wu KH, Yu CH, Chang YC, Horng DN (2004) Effect of pH on the formation and combustion process of sol–gel auto-combustion derived NiZn ferrite/SiO₂ composites. *J Solid State Chem* 177:4119–4125
 28. Tian C, Liu J, Cai J, Zeng Y (2008) Direct synthesis of La_{0.33}Si₆O₂₆ultrafine powder via sol–gel self-combustion method. *J Alloy Compd* 458:378–382
 29. Zhong Z, Ye N, Wang H, Ma Z (2011) Low temperature combustion synthesis and performance of spherical 0.5Li₂MnO₃–LiNi_{0.5}Mn_{0.5}O₂ cathode material for Li-ion batteries. *Chem Eng J* 175:579–584
 30. Sontakke S, Mohan C, Modak J, Madras G (2010) Visible light photocatalytic inactivation of E. coli with combustion synthesized TiO₂. *Chem Eng J*. doi:10.1016/j.cej.2012.02.036
 31. Chung SL, Wang CM (2011) A sol–gel combustion synthesis method for TiO₂ powders with enhanced photocatalytic activity. *J Sol–Gel Sci Technol* 57:76–85
 32. Yue Z, Zhou J, Li L, Zhang H, Gui Z (2000) Synthesis of nanocrystalline NiCuZn ferrite powders by sol–gel auto-combustion method. *J Magn Magn Mater* 208:55–60
 33. Deka S, Joy PA (2006) Characterization of nanosized NiZn ferrite powders synthesized by an autocombustion method. *Mater Chem Phys* 100:98–101
 34. Slatineanu T, Iordan AR, Palamaru MN, Caltun OF, Gafton V, Leontie L (2011) Synthesis and characterization of nanocrystalline Zn ferrites substituted with Ni. *Mater Res Bull* 46:1455–1460
 35. International Agency for Research on Cancer (2000) Diethanolamine: IARC monographs on the evaluation of carcinogenic risk to humans, vol 77. IARC Press, Lyon
 36. Cheremisinoff N (2003) Hazardous and toxic chemical profiles: industrial solvents handbook, 2nd edn. Marcel Dekker, Inc., New York
 37. Hwang CC, Tsai JS, Huang TH (2005) Combustion synthesis of Ni–Zn ferrite by using glycine and metal nitrates—investigations of precursor homogeneity, product reproducibility, and reaction mechanism. *Mater Chem Phys* 93:330–336
 38. Niasari MS, Davar F, Farhadi M (2009) Synthesis and characterization of spinel-type CuAl₂O₄ nanocrystalline by modified sol–gel method. *J Sol–Gel Sci Technol* 51:48–52
 39. Yuan T, Wei Z, Yuan J, Yan L, Liu Q, Wang J (2011) The microstructure and magnetic properties of Ni_{0.4}Zn_{0.6}Fe₂O₄ films prepared by spin-coating method. *J Sol–Gel Sci Technol* 58:501–506
 40. Atif M, Nadeem M, Grossinger R, Turtelli RS (2011) Studies on the magnetic, magnetostrictive and electrical properties of sol-gel synthesized Zn doped nickel ferrite. *J Alloy Compd* 509:5720–5724
 41. Barati MR (2009) Characterization and preparation of nanocrystalline MgCuZn ferrite powders synthesized by sol–gel auto-combustion method. *J Sol–Gel Sci Technol* 52:171–178
 42. Raghavender AT, Biliskov N, Skoko Z (2011) XRD and IR analysis of nanocrystalline Ni–Zn ferrite synthesized by the sol–gel method. *Mater Lett* 65:677–680
 43. Shirsath SE, Toksha BG, Kadam RH, Patange SM, Mane DR, Jangam GS, Ghasemi A (2010) Doping effect of Mn²⁺ on the magnetic behavior in Ni–Zn ferrite nanoparticles prepared by sol–gel auto-combustion. *J Phys Chem Solids* 71:1669–1675
 44. Mohammed KA, Al-Rawas AD, Gismelseed AM, Sellai A, Widatallah HM, Yousif A, Elzain ME, Shongwe M (2012) Infrared and structural studies of Mg_{1-x}Zn_xFe₂O₄ ferrites. *Phys B* 407:795–804
 45. Kambale RC, Shaikh PA, Harale NS, Bilur VA, Kolekar YD, Bhosale CH, Rajpure KY (2010) Structural and magnetic properties of Co_{1-x}Mn_xFe₂O₄ (0 ≤ x ≤ 0.4) spinel ferrites synthesized by combustion route. *J Alloy Compd* 490:568–571
 46. Zhao DL, Lv Q, Shen ZM (2009) Fabrication and microwave absorbing properties of Ni–Zn spinel ferrites. *J Alloy Compd* 480:634–638
 47. Bobade DH, Rathod SM, Mane ML (2012) Sol–gel auto-combustion synthesis, structural and enhanced magnetic properties of Ni²⁺ substituted nanocrystalline Mg–Zn spinel ferrite. *Phys B* 407:3700–3704
 48. Bueno AR, Gregori ML, N'obrega MCS (2007) Effect of Mn substitution on the microstructure and magnetic properties of Ni_{0.50-x}Zn_{0.50-x}Mn_{2x}Fe₂O₄ ferrite prepared by the citrate–nitrate precursor method. *Mater Chem Phys* 105:229–233
 49. Callister WD (2007) Magnetic properties: Materials Science and Engineering: An Introduction, 7th edn. Wiley, New York
 50. Cullity BD, Graham CD (2009) Ferrimagnetism: introduction to magnetic materials, 2nd edn. Wiley, New York
 51. Laokul P, Maensiri S (2009) Aloe vera solution synthesis and magnetic properties of Ni–Cu–Zn ferrite nanopowders. *J Optoelectron Adv Mater* 11:857–862
 52. Jahanbin T, Hashim M, Matori KA, Waje SB (2010) Influence of sintering temperature on the structural, magnetic and dielectric properties of Ni_{0.8}Zn_{0.2}Fe₂O₄ synthesized by co-precipitation route. *J Alloy Compd* 503(2010):111–117
 53. Xu X, Shen X, Zhu G, Jing L, Liu X, Chen K (2012) Magnetically recoverable Bi₂WO₆–Fe₃O₄ composite photocatalysts: fabrication and photocatalytic activity. *Chem Eng J*. doi:10.1016/j.cej.2012.06.104
 54. Casbeer E, Sharma VK, Li XZ (2012) Synthesis and photocatalytic activity of ferrites under visible light: a review. *Sep Purif Technol* 87:1–14
 55. Natarajan TS, Thomas M, Natarajan K, Bajaj HC, Tayade RJ (2011) Study on UV-LED/TiO₂ process for degradation of Rhodamine B dye. *Chem Eng J* 169:126–134
 56. Tehrani FS, Daadmehar V, Rezakhani AT, Akbarnejad RH, Gholipour S (2012) Structural, magnetic, and optical properties of zinc- and copper- substituted nickel ferrite nanocrystals. arXiv: 1203.3924v1